AIChE WILEY InterScience DISCOVER SOMETHING GREAT

Hydrodynamics of the Mixing Chamber in RIM: PIV Flow-Field Characterization

Ricardo J. Santos, Ertugrul Erkoç, and Madalena M. Dias
Laboratory of Separation and Reaction Engineering, Chemical Engineering Dept., Faculdade de Engenharia da Universidade do Porto, Porto 4200-465, Portugal

André M. Teixeira
Fluidinova—Engenharia de Fluidos S.A., Portugal

José Carlos B. Lopes
Laboratory of Separation and Reaction Engineering, Chemical Engineering Dept., Faculdade de Engenharia da Universidade do Porto, Porto 4200-465, Portugal, and Fluidinova—Engenharia de Fluidos S.A., Portugal

DOI 10.1002/aic.11472
Published online March 17, 2008 in Wiley InterScience (www.interscience.wiley.com).

The flow-field in a Reaction Injection Moulding, RIM, machine mixing chamber was characterized using the Particle Image Velocimetry (PIV) technique. This study covered the industrial range of Reynolds numbers, *Re*, for the RIM process, from 100 to 500, setting the overall trends of the flow-field in that range, with particular focus on the flow regime transition range of $100 \leq Re \leq 150$. The instantaneous 2D velocity vector maps were obtained with PIV in a plane containing the chamber and injectors axis. From instantaneous velocity data, the following quantities were computed: the probability density functions, the average velocity, and turbulence intensity. The present study sheds additional light into the transition of flow-field regime that marks the onset of mixing on RIM, and also into the mixing mechanisms and respective underlying flow-field features. © 2008 American Institute of Chemical Engineers *AIChE J,* 54: 1153–1163, 2008
Keywords: T-jets, T-mixer, opposing jets, mixing

Introduction

Confined Impinging Jets, CIJ, and similar opposed jets mixers are mainly used for mixing under fast chemical reaction processes, where the limiting step is the reactants contacting or mixing. Examples of opposed jets mixers usage are Reaction Injection Moulding (RIM),[1] T-micromixers,[2] opposed jets burners,[3,4] and precipitators.[5–7] The geometry and range of flow parameters of the present study are those typically found in the high-pressure RIM process. The mixing chamber used in this work with its dimensions is shown in Figure 1.

Correspondence concerning this article should be addressed to J. C. B. Lopes at lopes@fe.up.pt.

© 2008 American Institute of Chemical Engineers

In a previous work of our group[8] the flow-field in a RIM machine mixing chamber was characterized with Laser Doppler Anemometry (LDA). The LDA results were obtained in single points at each time, and so an overall image of the instantaneous flow-field was not possible to obtain. Here that initial work[8] is completed with Particle Image Velocimetry (PIV), measurements to measure the instantaneous 2D velocity vectors simultaneously at several points throughout a plane in the mixing chamber: velocity vector map.

Previous imaging works of the instantaneous flow-field in the mixing chamber of the RIM machine include tracer maps from the mixing of a dyed jet with a clear one[9–11]; images obtained from the injection at both jets of a fillet of a tracer that fades with mixing[12]; particle paths visualization[13]; and Laser Induced Fluorescence (LIF).[14,15] From these visualiza-

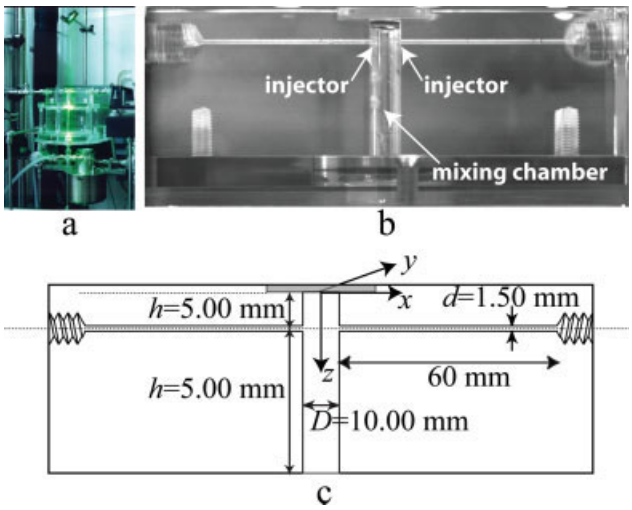

Figure 1. RIM machine mixing chamber.

(a) Photo of the mixing chamber and discharging mould lighted with the PIV laser sheet; (b) detailed photo of the mixing chamber, and (c) drawing of the mixing chamber with dimensions and the coordinate axes. [Color figure can be viewed in the online issue, which is available at www.interscience.wiley.com.]

tion studies the main conclusion was the existence of two very distinct flow regimes.

- *Segregated flow regime*, where both jets impinge at the mixing chamber axis and then flow outwards the chamber from their original inlet side. The segregated flow regime was very clearly imaged from tracer and LIF experiments,[10] where the mixing chamber is seen half colored and half blank, and the segregation plane is defined at the chamber axis in the normal direction to the injectors axis.
- *Self-sustainable chaotic flow regime*, where there is the formation of vortices immediately downstream the jets impingement point, which engulf both streams promoting a very fast homogenization inside the mixing chamber. Because of the fast homogenization that occurs for the self-sustainable chaotic flow regime the tracer studies[10] did not allow a clear image of mixing mechanisms. This flow regime is best visualized from particle studies, namely the work of Lee et al.[9] with aluminum powder tracer, or from particle paths studies.[13] CFD simulations of the advection of a tracer in RIM[16] clearly show the presence of Lagrangian chaos for this flow regime, although the proof of Eulerian chaos existence is not yet published.

The experimental characterization of self-sustainable chaotic flow regime is hitherto not clear from the available literature. Previous experimental works, which were mostly published more than a decade ago, had been affected by the very fast flow homogenization.[9,13,15] In the present work the flow-field in the RIM mixing chamber is characterized with unprecedented detail, by the use of a technique not previously reported on this particular type of mixer, and which is not affected from fast homogenization or the mixing history: PIV. The use of PIV allows in addition to the flow structures imaging, which was also possible to some extent in earlier works,[9,13,15] the quantification of the local velocities for a more accurate validation of CFD simulations results.

This work also adds to the published literature the thorough visualization of the flow-field evolution with Reynolds numbers ranging from 100 to as high as 500. Previous visualization works reported Reynolds numbers up to: $Re = 252$,[10] $Re = 150$,[9] $Re = 118$,[13] $Re = 74$,[14] and $Re = 81$.[15] Sandell et al.[12] made visualization studies in the range of $155 \leq Re \leq 640$, using water as the fluid and thus the Froude numbers are lower than those typical of RIM, which seriously compromise the flow dynamics as clearly shown by Santos et al.[17] Furthermore, in Sandell et al.[12] the mixing chamber has dimensions that are 10 times those of a RIM mixing chamber, and the impinging jets form a 130° angle pointed towards the chamber closed top and are not directly opposed.

Other visualization studies were obtained in mixer geometries close to the RIM mixing chamber, namely, on confined impinging jets precipitators[18–21] and on micro mixers.[22,23] The mixing mechanisms in both types of mixers are different than in RIM, even though the Reynolds numbers are approximately in the same range. For the case of the micro mixers the scale of the reactor prevents the formation of the vortices that engulf both jets, and the flow is segregated in two halves.[22,23] Wong et al.[22] showed that the vortices in T-jets micro mixers have the rotation axis parallel to the main flow direction, while in RIM the vortices rotation axis is perpendicular.[16] In the precipitators the mixer dimensions are at least tenfold than in RIM, and so the vortices scales are not geometrically constrained by the chamber. In RIM the vortices are formed in pairs of counter rotating vortices each occupying half the chamber diameter whereas in a T-jets precipitator[18] this fixed scale it is not observable. For smaller precipitators[6,24] the dimensions and flow conditions are closer to RIM mixing chamber, but visualization or other experimental fluid mechanics works are not yet available.[7]

In most of the previous works on this subject the same fluid was used on both jets. In industrial RIM processes, one stream is a polyol and the other an isocyanate, and the occurrence of complex interfacial phenomena[25] may also have some effect on mixing.[26] Nevertheless, this works fills a gap in literature regarding the characterization of the flow-field in the RIM machine mixing chamber, aiming the validation of CFD simulations results[16] and the identification of the mixing mechanisms in the RIM process.

Experimental Setup

Mixing chamber

The RIM machine setup for the PIV experiments was presented in a previous publication,[8] where a stainless steel mixing chamber was used and here was replaced by a new transparent acrylic chamber shown in Figure 1. The dimensions of the transparent mixing chamber, which are the same than the previous works,[8,17] and the reference axis for results presentation, are also shown in Figure 1.

The transparent mixing chamber was made from a single acrylic block that was drilled from side to side in order to guarantee the perfect jets alignment. In Figure 1b it is shown a detailed photo of the mono-block where the jets and chamber were drilled. The injectors have a diameter d of 1.50 mm, the mixing chamber diameter, D, is 10.00 mm and the chamber height, H, is 50 mm. The injectors are perpendicular to

the chamber and its centre is located at a distance $h = 5.00$ mm of the mixing chamber closed top. The injectors have a length of $h = 5.00$ mm to ensure a fully developed Poiseuille flow at the mixing chamber entrance.

Fluids

The fluid used in the experiments is a glycerine aqueous solution. General expressions for density and viscosity were obtained from experimental characterization of the glycerine aqueous solutions at our laboratory. The expression for density is,

$$\rho = \left(1 - X_{\text{glycerine}}\right)\rho_{\text{water}} + X_{\text{glycerine}}\rho_{\text{glycerine}} \tag{1}$$

where $X_{\text{glycerine}}$ is the glycerine mass fraction, $\rho_{\text{water}}(\text{kg/m}^3)$ and $\rho_{\text{glycerine}}(\text{kg/m}^3)$ are the water and glycerine densities respectively, which are functions of the temperature, θ (K)

$$\rho_{\text{water}} = 1064.60 - 0.23\theta \tag{2}$$

$$\rho_{\text{glycerine}} = 1440.50 - 0.61\theta \tag{3}$$

For the viscosity, the following expression was obtained from experimental data obtained with a UDS 200 PaarPhysica rotational rheometer in the ranges of $20^{\circ}\text{C} \le \theta \le 25^{\circ}\text{C}$ and $0 \le X_{\text{glycerine}} \le 88\%$,

$$\mu = \left((1 - X_{\text{glycerine}})\left(A_{\text{water}}\text{e}^{\frac{B_{\text{water}}}{\theta}}\right)^a + X_{\text{glycerine}}\left(A_{\text{glycerine}}\text{e}^{\frac{B_{\text{glycerine}}}{\theta}}\right)^a\right)^{1/a} \tag{4}$$

where μ is the viscosity in mPa s, and the constants are equal to: $A_{\text{water}} = 5.17 \times 10^{-4}$ mPa s, $B_{\text{water}} = 2.22 \times 10^3$K, $A_{\text{glycerine}} = 7.06 \times 10^{-9}$ mPa s, $B_{\text{glycerine}} = 7.64 \times 10^3$K, $a = -0.320$.

In the present work a glycerine aqueous solution with $X_{\text{glycerine}} = 72.2\%$ was always used, which at a temperature close to the experimental conditions, 22°C, has $\rho = 1187\text{kg/m}^3$ and $\mu = 25.2$mPa s.

The viscosity and density curves as functions of temperature were used to calculate the Reynolds number, *Re*, originally defined for RIM machine mixing chamber at the injector as,[27]

$$Re = \frac{\rho \upsilon_{\text{inj}} d}{\mu} \tag{5}$$

where υ_{inj} is the superficial velocity at the injectors, d the injectors diameter, ρ the fluid density and μ the fluid viscosity. The superficial velocity, υ_{inj}, is computed from the flow rate at each injector divided by the injector cross sectional area. The complete list of experimental conditions for each *Re*, based on the fluid properties at the operation temperature, is presented in Santos.[28]

The maximum experimental error associated to the Reynolds number was measured[28] and set to 10%. The error was determined from setting the Reynolds number in the pilot RIM control graphic interface and then measuring the actual Reynolds number from the flow rate and fluid temperature.

PIV system

For the PIV measurements the fluids were seeded with nylon particles with 4 μm in diameter (TSI, pt-900845). The PIV setup computed 2D velocity fields from the displacement of the seeding particles between two images obtained at consecutive time instants. The PIV laser sheet was emitted by a 12 mJ Nd:Yag laser from New Wave Research (model Mini-Laser—15) having two laser cavities, so the time gap between consecutive pulses can be set to values as small as 1 μs. Each laser is pulsed at 15 Hz which induces the lighting of each frame of a pair of frames.

The emitted laser beam has a diameter of 2.5 mm that is converted into a sheet through a combination of a −25.0 mm cylindrical lens and a 200 mm spherical lens, yielding a sheet of 17.5 mm height and 50.9 μm thickness at a distance of 20 mm from the lenses, which is approximately half the length of the sheet path from the laser to the chamber.

The other PIV system components are: a CCD camera, PIVCAM 10–30 from TSI, with 1016 × 1024 pixels CCD and a frame rate of 30 Hz; a synchroniser (TSI model 610032), which is in control of all the processes, giving the signals to the laser for flash and reading the PIVCAM shutter opening exact time.

Figure 2 shows two images acquired by the PIV camera for the vector maps computation, which was performed with the software Insight, from TSI. Each image corresponds to one of the imaged domains from the two sets of experiments that will be presented. The images are obtained in pairs and the particles displacement, between two consecutive frames, is computed in Insight by using a cross-correlation method. In this method, the consecutive frames, grouped in pairs, are divided in several squares, interrogation spots, and each interrogation spot is correlated to the interrogation spot at the consecutive frame having the same location. From the cross-correlation of the interrogation spots having the same location a displacement vector is obtained, the velocity vector is computed from the displacement vector and the time interval between the two consecutive frames. Figure 2 shows the dimensions of the interrogation spots on the imaged domains.

The seeding pattern of the lighted field that is shown in Figure 2 corresponds to the description of the good seeding conditions for PIV.[29]

Vector validation

Spurious velocity vectors in PIV measurements result from mismatching of the particle patterns between the interrogation spot in the frames of each pair.[30] Therefore, spurious vectors are characterized by a small correlation peak. These spurious vectors are due to insufficient seeding, strong velocity gradients, and three-dimensional motion of the particle out of the laser sheet plane. These vectors generally present a discontinuity in the vector maps and are, therefore, of easy identification.[30,31] Their elimination is based on comparison procedures with the surrounding vectors. In the present work the vector validation was made by setting the maximum deviation a vector could present to six times the standard deviation computed from all the vectors in that map.

Experiments

Two sets of experiments were performed, labeled Set 1 and Set 2. The Set 1 experiments consist of PIV measurements for *Re* values between 100 to 500 with intervals of $Re = 100$. The purpose was to draw the overall variation of

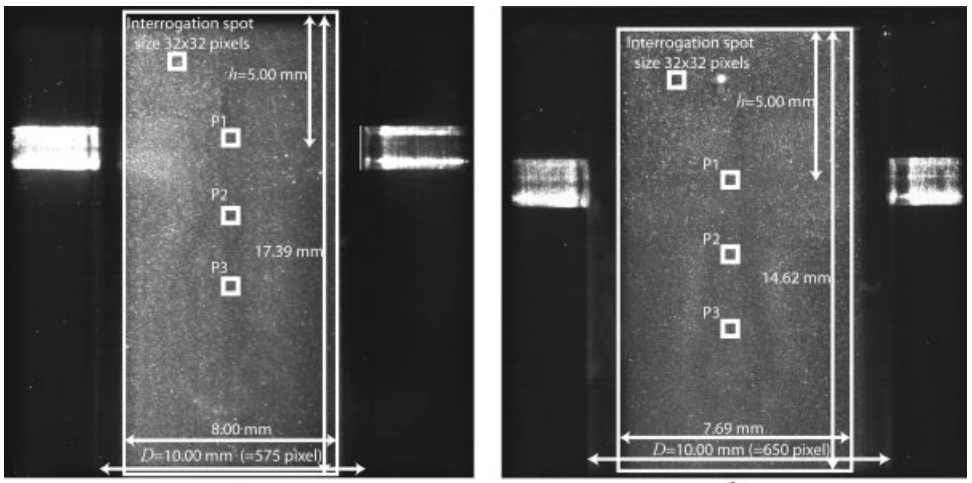

Figure 2. Frame from the PIV camera of the mixing chamber for experiments of (a) Set 1 and (b) Set 2.

The frames show a square delimiting the processed region and its dimensions in both pixels and millimeters.

the flow-field with *Re* and its statistics. The Set 2 experiments were focused on the *critical Reynolds number* phenomenon, which marks the transition between segregated and chaotic flow regime, and so PIV measurements were done with intervals of 5 from $Re = 100$ to $Re = 130$, and with intervals of 10 from $Re = 130$ to $Re = 150$. The experimental conditions for both sets of experiments are listed in detail by Santos.[28]

Figure 2 shows a frame from each set of experiments with the dimensions of the processed region, of the interrogation spot and the location of some interrogation spots labeled P1, P2, and P3.

Each frame has 1016 (width) × 1024 (height) pixels, so the measurement area is approximately square, while the mixing chamber has a ratio of five between the height and the diameter, $H/D = 5$. To maximize the number of pixels in the area where the flow dynamics is known to be stronger from the previous LDA experiments[8] the measurements were done only in the top 17.4 mm of the chamber, for Set 1 experiments, and in the top 14.6 mm for Set 2 experiments since a greater detail of the flow was intended to visualize the mechanisms marking the onset of the chaotic flow regime.

For the Set 1 five batch acquisitions of 200 frame pairs were taken for all *Re* except $Re = 500$ for which eight batch acquisitions were made. In the Set 2 experiments a single batch of 200 pairs of images was acquired for each *Re*.

For both sets of experiments the problem of image distortion due to the cylindrical shape of the chamber was solved by closely matching the refraction index of the fluid to that of the acrylic. A study of the optic effects in the chamber is presented by Santos.[28]

Near the mixing chamber walls, for both sets of experiments, the image is unclear, as shown in Figure 2. This is not due to optical effects, but rather to an illumination problem since the shadow projected by an O-ring positioned in the upper part of the mixing chamber has limited the illuminated area to the central region. There is a margin of 1.00 mm and 1.15 mm of shaded area, in Set 1 and Set 2, respectively, where it is not possible to compute the velocities because there are no visible particles. Therefore only the central part of the chamber is measured, which further reduces the effect of the already small optical distortion affecting the PIV data.

For the PIV experiments two parameters must be set:

- the time interval between the frames of each pair, Δt_F;
- the size of the interrogation spot.

The criterion for setting the time between two consecutive frames is that the particles move less than a fourth of the interrogation spot width. The value of the time interval between two frames of the same pair, Δt_F, was set from the extreme values of the velocity. The displacement of the particles in pixels is

$$\Delta x = (\upsilon \Delta t_F) F_{pixel} \tag{6}$$

where υ is the particle velocity and F_{pixel} is the conversion factor between meters and pixels and is obtained by

$$F_{\text{pixel}} = \frac{D_{\text{pixels}}}{D_{\text{m}}} \tag{7}$$

where D_{pixels} and D_{m} are the chamber diameter in pixels and meters, respectively. For Set 1 $F_{\text{pixel}} = 5.75 \times 10^4$[pixel/m] and for Set 2 $F_{\text{pixel}} = 6.50 \times 10^4$[pixel/m]. The values of the particle displacement in pixels were calculated considering that $\upsilon = \upsilon_{inj}$ and are presented in Tables 1 and 2 for Set 1 and 2, respectively.

The interrogation spot for both experiments was a square of 32 × 32 pixel. The criterion of a displacement less than one fourth of the interrogation spot size, that is, up to 8 pixels, is more than accomplished by the chosen values of Δt_F. If the maximum velocity is considered, $2 \times \upsilon_{\text{inj}}$, the value of Δx is most of the times still within the limiting range for Δt_F as can be easily computed from Tables 1 and 2 data.

The flow-field becomes more heterogeneous for higher values of *Re*, with extreme changes of the velocity directions in short periods and distances, and so three different values of Δt_F were used at $Re = 500$ (see Table 1). The lower values of Δt_F allow a better imaging of the flow-field near the jets impingement point where the velocity gradients are extreme. At the other regions of the flow-field the particles displacement is very small for the lower values of Δt_F and so higher

Table 1. Experimental Conditions and PIV Parameters for Set 1 Experiments

	Batch	θ [°C]	υ_{inj} [m/s]	Δx [pixel]	Δt_F [μs]
$Re = 100$	1	21.5	1.43	4.1	50
	2	21.9	1.40	4.0	
	3	21.6	1.42	4.1	
	4	21.9	1.40	4.0	
	5	22.6	1.37	3.9	
$Re = 200$	1	21.7	2.83	4.1	25
	2	21.5	2.85	4.1	
	3	22.1	2.79	4.0	
	4	22.5	2.75	3.9	
	5	22.0	2.80	4.0	
$Re = 300$	1	22.3	4.15	3.6	15
	2	22.1	4.18	3.6	
	3	21.7	4.25	3.7	
	4	21.7	4.25	3.7	
	5	22.0	4.20	3.6	
$Re = 400$	1	22.7	5.45	5.45	12
	2	23.2	5.35	5.35	
	3	21.9	5.62	5.62	
	4	21.6	5.68	5.68	
	5	21.9	5.62	5.62	
$Re = 500$	1	21.9	7.02	4.8	12
	2	22.2	6.94	4.8	
	3	21.5	7.13	4.1	10
	4	21.9	7.02	2.0	5
	5	22.3	6.92	2.0	
	6	22.6	6.84	2.0	
	7	22.7	6.81	2.0	
	8	22.4	6.89	2.0	

values of Δt_F were used to depict the flow-field in these regions.

Calculated quantities

From the PIV measurements the following quantities were calculated: instantaneous velocity field; turbulence intensity field; average turbulence intensity; probability density function, pdf, of υ_x at a point.

The dimensionless turbulence intensity was computed for the x and the z components of the velocity, σ_x^* and σ_z^*, respectively at each point as

$$\sigma_x^* = \frac{1}{\upsilon_{inj} n_{samples}} \sqrt{\sum_{i=1}^{n_{samples}} \left(\upsilon_x(i) - \langle \upsilon_x \rangle\right)^2} \tag{8}$$

$$\sigma_z^* = \frac{1}{\upsilon_{inj} n_{samples}} \sqrt{\sum_{i=1}^{n_{samples}} \left(\upsilon_z(i) - \langle \upsilon_z \rangle\right)^2} \tag{9}$$

where υ_{inj} is the jets superficial velocity at the injectors, $n_{samples}$ is the total number of time instants computed, $\upsilon_x(i)$ and $\upsilon_z(i)$ is the i^{th} measurement of velocity components x and z, and $\langle \upsilon_x \rangle$ and $\langle \upsilon_z \rangle$ are the average value of $\upsilon_x(i)$ and $\upsilon_z(i)$.

The spatial average of the turbulence intensity for each component was calculated as

$$\overline{\sigma^*} = \frac{\sum_{i,j=1}^{n_{points}} \sigma^*(i,j) \Delta x_i \Delta z_j}{\sum_{i=1}^{nx_{points}} \Delta x_i \sum_{j=1}^{nz_{points}} \Delta z_j} \tag{10}$$

where Δx_i and Δz_j are the interrogation spot dimensions, nx_{points} and nz_{points} are the number of interrogation spots in the x and the z direction, respectively, and $n_{points} = nx_{points} \times nz_{points}$ is the total number of interrogation spots. Although the flow-field characterization is also done resorting to a quantity called turbulence intensity, the flow is laminar and chaotic.

The successive x component velocity data at a specific point was extracted from the PIV measurements, and to get greater insight of the evolution of the flow-field behavior in the Set 2 experiments its pfd was computed at the points P1, P2, and P3, see Figure 2. The pdf of υ_x^* is defined as

$$p(\upsilon_x^*) = \frac{n_{sample}\big|_{\upsilon_x^* \le \upsilon^* < \upsilon_x^* + \Delta\upsilon^*}}{n_{sample} \Delta\upsilon^*} \tag{11}$$

where $n_{sample}\big|_{\upsilon_x^* \le \upsilon^* < \upsilon_x^* + \Delta\upsilon^*}$ is the number of samples of υ_x^* belonging to the interval $[\upsilon_x^*;\upsilon_x^* + \Delta\upsilon_x^*]$, n_{sample} is the total number of samples and $\Delta\upsilon^*$ is the width of each class in the *pfd*. $p(\upsilon_x^*)$ is the probability that υ_x^* belongs to the interval $[\upsilon_x^*;\upsilon_x^* + \Delta\upsilon_x^*]$ where υ_x^* is the dimensionless υ_x and is defined as

$$\upsilon_x^* = \frac{\upsilon_x}{\upsilon_{inj}} \tag{12}$$

Flow-Field Characterization

The description of the instantaneous flow-field is done by presenting snapshots of representative velocity vector maps for each Reynolds number, which allows a direct observation of the flow-field. All the maps from PIV measurements presented are limited by a dashed line box around the measured area. The measured area does not cover the whole diameter of the mixing chamber due to the shading region near the walls, as seen from Figure 2. The dashed line box is inserted inside a frame representing the mixing chamber boundaries.

The results are presented on a single plane and so a complete picture of the flow-field inside the chamber is not given. Nevertheless the chosen plane is the one where the flow presents the strongest dynamics,[8] and the main mixing mechanisms.[16]

The results from both sets of PIV experiments, Set 1 and Set 2, are presented separately. Set 1 experiments are presented first, drawing the general flow-field evolution with the Reynolds numbers between $Re = 100$ and $Re = 500$. The second set of experiments, Set 2, is presented for a detailed

Table 2. Experimental Conditions and PIV Parameters for Set 2 Experiments

Batch	θ [°C]	υ_{inj} [m/s]	Δx [pixel]	Δt_F [μs]
$Re = 100$	22.5	1.37	3.9	50
$Re = 105$	22.5	1.44	4.1	
$Re = 110$	22.7	1.50	4.3	
$Re = 115$	22.7	1.57	4.5	
$Re = 120$	22.5	1.65	4.7	
$Re = 125$	22.8	1.70	4.9	
$Re = 130$	22.9	1.76	5.1	
$Re = 140$	23.0	1.89	5.4	
$Re = 150$	23.0	2.02	4.6	40

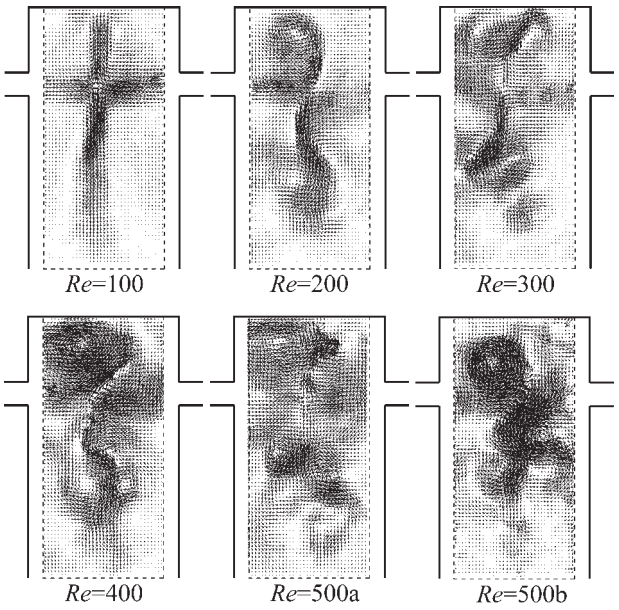

Figure 3. 2D instantaneous velocity vector maps from the experiments of Set 1 for *Re* = 100 to *Re* = 500.

Re = 500a was taken with Δt_F = 12 μs and *Re* = 500b with Δt_F = 5 μs (see Table 1).

characterization of the flow-field evolution in the range of Reynolds numbers where the most dramatic changes in the flow-field occur, $100 \leq Re \leq 150$.[9,10,13,15]

Overall effect of the Reynolds number

The first approach to the problem from PIV experiments was to depict the evolution of the flow structures for the Reynolds number range of industrial interest. This approach is only qualitative, and the second step, towards quantification, was the computation of the intensity of turbulence to measure the changes in the flow-field at several Reynolds numbers.

Instantaneous Velocity Field. Figure 3 shows a representative velocity vector map for each Reynolds numbers of Set 1 experiments. From the vector maps of Figure 3 at *Re* = 100 a segregated flow regime is observed. The main characteristic of the flow-field at this Reynolds number is the preferential flowing through the chamber axis creating a shortcut to the outlet. The axial flow is generated by the jets impingement at the chamber axis; afterward the jets bend and are directed towards the outlet keeping their high velocity. This flow in the axial region is characterized by a very weak lateral velocity[15] keeping the two halves of the mixing chamber segregated as seen from previous visualization experiments.[10,14] Between the axial flow with high velocity and the wall there are two zones of recirculation. The flow near the wall takes the opposite direction of the axial flow, giving rise to two elongated vortices, one in each side of the chamber. In the regions upstream the jets, two symmetric vortices are formed, keeping a very well defined shape and are practically undisturbed by the jets. Because of the reduced interaction with the neighboring flow structures it is most likely that the fluid almost trapped in those closed vortices presents extremely high residence times when compared to the chamber average residence time.[16] The overall velocity pattern here identified at *Re* = 100 is consistent with the particle paths at the segregated flow regime observed by Wood et al.,[13] at *Re* = 60.5, and by Unger and Muzzio[19] in a precipitator at *Re* = 40.

The velocity vector maps at *Re* = 200, presented in Figure 3, clearly show the dramatic change in flow-field from *Re* = 100 to *Re* = 200, where a self sustainable chaotic flow regime now occurs. At *Re* = 200 the jets impinge on each other close to the chamber axis and are directed towards the outlet. The preferential path, through chamber axis towards the outlet, is broken by the formation of circular vortices downstream the injectors. The interface between both sides of the mixing chamber loses definition and its location changes strongly with time.[8] The main feature of the flow at *Re* = 200, is the formation of the downstream vortices that promote the engulfment of the jets with the surrounding fluid. The upper vortices symmetry is dynamically broken, indicating that the jets oscillation amplitude has considerably increased from *Re* = 100 to *Re* = 200. The velocity pattern at *Re* = 200 is consistent with the particle paths at the chaotic flow regime, *Re* = 118, observed by Wood et al.[13] and with the tracer patterns observed by Lee et al.[9] at *Re* = 150.

The same overall behavior of the flow, with the formation of vortices downstream the injectors can be seen for *Re* = 300 from the vector maps in Figure 3. Three important differences are observed:

- the vortices are formed near the impingement point and evolve further in the chamber without losing their identity;
- the interface segregating the two sides of the mixing chamber is further distorted;
- the upper vortices are even more distorted by the jets oscillations.

This list shows that all the changes have gone towards a stronger dynamics of the flow-field.

The results from the measurements at *Re* = 400 and 500, also shown in Figure 3, presented the same trends identified from *Re* = 200 to *Re* = 300 towards a stronger dynamics of the flow. The main evolution on the system is the formation of vortices before the jets impinge on each other, which is even clearer at *Re* = 500 and goes in the already identified trend of vortex formation near the jets.

For the characterized flow regimes above *Re* = 100 it is always observed the formation of vortices immediately downstream the jets with a typical diameter equal to half the mixing chamber diameter. The formation of these vortices corroborates the predicted flow structures from the 2D Computational Fluid Dynamic (CFD), simulations of the mixing chamber.[16,17]

In the mentioned previous characterization works of the RIM mixing chamber flow-field, the flow was always imaged from tracer maps or particle paths. This work presents for the first time the actual hydrodynamics of instantaneous flow-field as 2D vector maps, at a plane located in the mixing chamber and injectors axis.

Turbulence Intensity. In Figure 4 the maps of the *x* and *z* components of the dimensionless turbulence intensity, σ_x^* and σ_z^*, for *Re* = 100 to *Re* = 500 are presented. The scale of the color bar for the *Re* = 100 maps is half of that for the

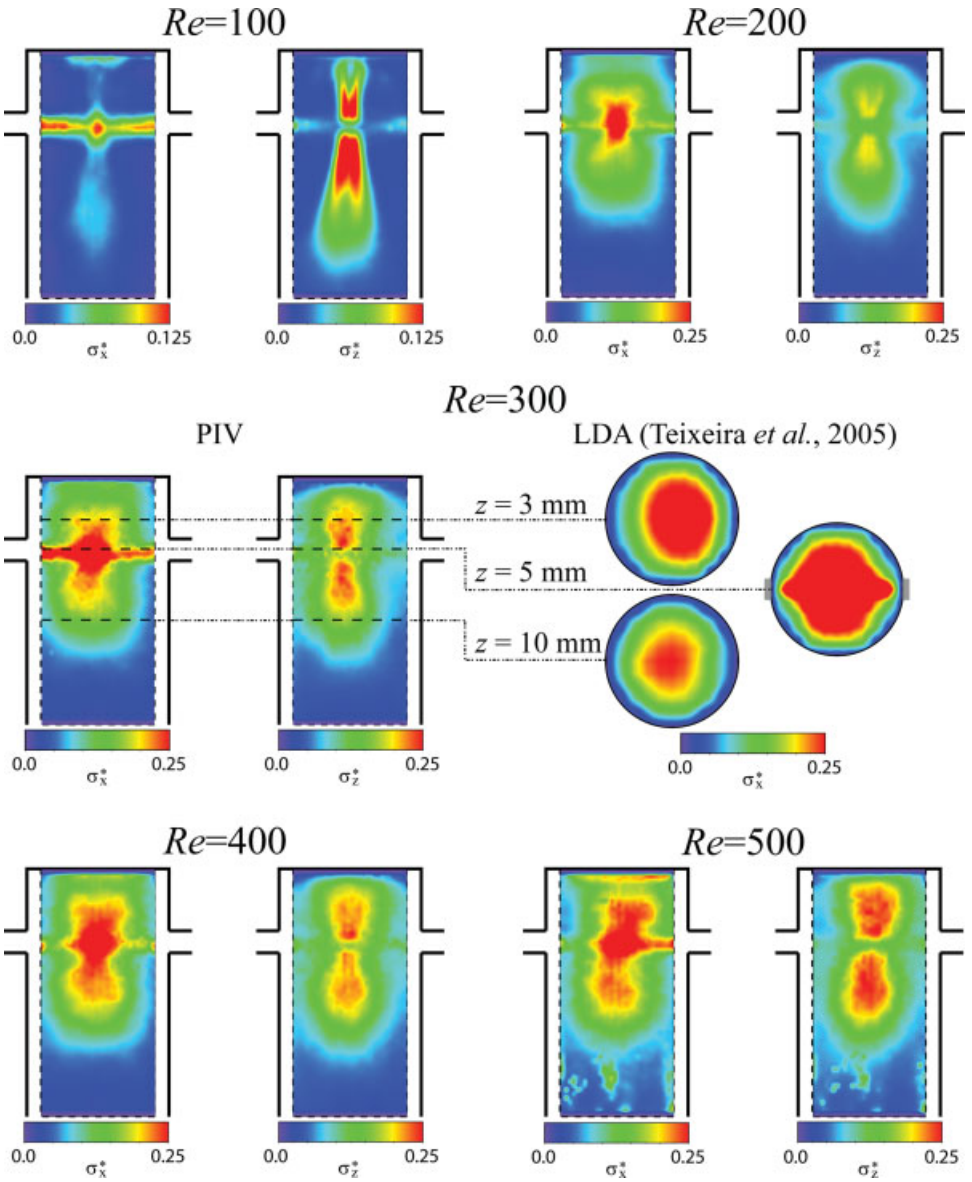

Figure 4. Turbulence intensity maps, σ_x^* and σ_z^*, from the PIV experiments of Set 1 for *Re* = 100 to *Re* = 500 in the *xz* plane containing chamber and injector axes.

Turbulence intensity maps, σ_x^*, from LDA measurements of Teixeira et al.[8] at $Re = 300$ in xy planes located at $z = 3$, 5, and 10 mm. [Color figure can be viewed in the online issue, which is available at www.interscience.wiley.com.]

other Reynolds numbers due to the lower values of σ_x^* and σ_z^* at this Reynolds number.

From the turbulence intensity maps it is possible to identify an evolution from the lowest to the highest value of the Reynolds numbers in the experiments. The intensity of turbulence gives a measure of the velocity component fluctuations and since it is normalized by the jets superficial velocity, the maps of σ_x^* and σ_z^* at different values of *Re* are directly comparable. The regions of higher fluctuations are directly associated with mixing mechanisms since the fluctuations promote the transport of fluid to the surrounding regions and thus, the intensity of turbulence, can also be seen as a scale of the mixing dynamics. Further the maps of σ_x^* and σ_z^* present the regions where the flow variation with time, flow dynamics, is stronger, thus providing insight into the genesis of the strong convective mixing mechanisms in the RIM mixing chamber.

From Figure 4 it is seen that, at $Re = 100$, the flow fluctuations are mainly along the injectors axis for the x velocity component, υ_x, and in the chamber axis for z velocity component, υ_z. The flow outside the injectors and chamber axis presents very little time dependence. The values of σ_x^* at $Re = 100$ are at least three times smaller than for higher values of Reynolds number. These low values of σ_x^* indicate very weak lateral oscillations and consequently a high degree of vertical segregation in the mixing chamber. The weak flow fluctuations at $Re = 100$ show some time dependence with small amplitude oscillations, which was already known from previous works.[13,14]

From the intensity of turbulence maps at $Re > 100$, it can be seen that the predominant fluctuations are in the x direction and thus promoting a strong dynamics of mass transfer in the direction normal to the average flow. Similarly to $Re = 100$, for the other Reynolds numbers, the highest values of σ_x^* are at the impingement point and along the jets, but some differences in the distribution of higher values of σ_x^* are observed. The highest values of σ_x^* are not concentrated along the chamber and jets axes, rather there is a concentric distribution with the highest values at the impingement point and smoothly decreasing from there on. The regions of higher values of σ_x^* increase with the Reynolds number, being expanded to greater distances downstream of the jets up to $Re = 500$.

The values of σ_z^* present the same overall distribution than σ_x^* with the difference of not having the highest values centered at the impingement point but in two points in the chamber axis: one above and the other below the jets. The region of lower values of σ_z^* in the jets line clearly shows that the jets fluctuations are mainly in the x direction. The jets impinge in the chamber axis being then bent to the z direction, and thus afterwards the impingement point, both up and down, the dynamics in the z direction reaches its peak.

Figure 4 also shows the σ_x^* maps at $Re = 300$ from the LDA results,[8] which were obtained in the normal direction to the PIV maps but using a fluid with higher viscosity, 60 mPa s. To compare the σ_x^* distributions in space, three lines cutting the xz plane at $z = 3$, 5 and 10 mm were defined and the planes from the LDA measurements at those positions shown.

The same patterns are seen in the σ_x^* maps from LDA and PIV measurements, although its values are slightly higher for the LDA measurements, probably due to: the higher jets velocity associated to the usage of more viscous fluids at the same $Re = 300$ in the LDA experiments[8]; or to the fact that the LDA measuring volume captures data in a wider range of horizontal xy planes, the LDA measuring volume has 2.4 mm in z direction against the 0.56 mm of the PIV interrogation spot for Set 1, thus at a fixed point the LDA measurements always include regions of higher dynamics closer to the jets impingement point. The results from both techniques allow a 3D picture of turbulence intensity distribution to be drawn. From the turbulence intensity maps it can be seen that the strongest velocity fluctuations occur near the jets impingement point and that they decrease from that point in all the three directions: x, y and z. Despite the strong dynamics of the flow in the x direction, the average maps of υ_x show that, a distance less than a mixing chamber diameter downstream the jets, the average values of υ_x are approximately zero.

Similar distributions of turbulence to the ones here presented were reported from 3D CFD simulations,[24] at $200 \leq Re \leq 400$ in a CIJR, and at much higher Reynolds numbers,[32] $Re = 35{,}000$, in a opposed jets mixer. The distribution pattern of turbulence intensity, peaking at the impingement point and decreasing radially towards x, y, and z, seems to be kept from the onset of the chaotic flow regimes to beyond the transition to fully developed turbulent regimes.

Figure 5 shows the plot of the space averaged values of σ_x^* and σ_z^*, $\overline{\sigma_x^*}$, and $\overline{\sigma_z^*}$, evolution with the Reynolds number from $Re = 100$ to 500. From this plot it is clear that there is a sharp increase of the turbulence values between Reynolds numbers 100 and 200 and a monotonically slower increase of the turbulence values above Reynolds number 200. This sharp evolution o the flow dynamics around a critical Reynolds number is associated to the transition from segregated flow regime to self-sustainable chaotic flow regime, a phenomenon widely known from the original RIM studies[9,10] and that will be analyzed in detail in the following section.

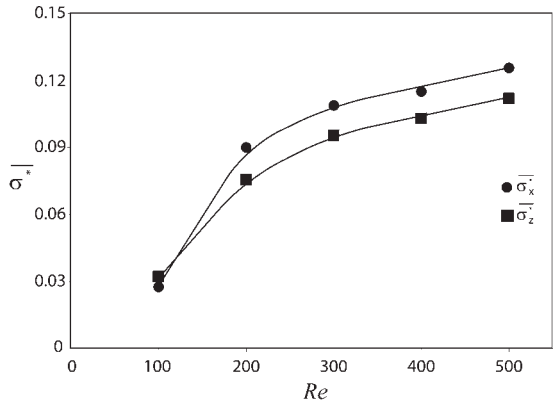

Figure 5. Plot of the variation of the *x* and *z* components of the average intensity of turbulence, σ_x^* and σ_z^*, with the Reynolds number for the Set 1 experiments.

The evolution of mixing or chemical reaction in RIM mixing chambers with the Reynolds[33–35] presents a similar trend to the turbulence intensity plots of Figure 5. The correlation between chemical reaction studies and the mixing/flow-field dynamics clearly shows that the fast mixing of the two opposed monomer streams is a key factor affecting the final properties of the high pressure RIM products.[36]

Critical Reynolds number characterization

Further PIV measurements, listed in Table 2, referred in this work as Set 2 were made with the purpose of sweeping the range of Reynolds number where the flow regime transition is known to occur. The interval between the Reynolds numbers is 5, from $Re = 100$ to $Re = 130$, and then, up to $Re = 150$, the interval is increased to 10 since the system is already beyond the flow regime transition or critical Reynolds number. In Set 2 experiments for each Reynolds number, only 200 frames were captured.

Instantaneous Velocity Field. The evolution of the flow-field with the Reynolds number is first depicted from the instantaneous velocity vector maps shown in Figure 6. From $Re = 100$ to 115, as previously observed for $Re = 100$ in Figure 3, there is a preferential jet flow through the chamber axis with the formation of an elongated vortex downstream the jets in each side of the chamber. Some evolution is seen from $Re = 100$ to 115 with an increasing trend to the formation of circular vortices downstream the jets that disturb the interface between the two streams and an increasing distortion of the upper vortices.

From $Re = 115$ to 120 a transition of the flow regime clearly occurs. The circular vortices that at $Re = 115$ slightly disturb the interface between both streams, at $Re = 120$ have

further evolved to completely distort the interface, which vanishes, as well as the preferential path toward the outlet. These dramatic changes in the flow-field are clear from the observation of Figure 6 and thus this study will set the critical Reynolds number at $Re = 120$, close to values previously reported.[9,10,13,15,27,35] For higher Reynolds numbers, from $Re = 120$ up to $Re = 150$ where the flow presents a strong dynamics, the flow-field features identifiable from the instantaneous velocity vector maps do not present any observable evolution with the Reynolds number.

Turbulence Intensity. Figure 7 shows the average values of $\overline{\sigma_x^*}$ and $\overline{\sigma_z^*}$ from Set 2 experiments. The average turbulence intensity values of Set 1 are slightly lower than those of Set 2 because for Set 1 the computed area includes regions further downstream in the mixing chamber and thus presenting lower values of σ_x^* and σ_z^*. For the values of Set 2 experiments a very slight increase, of about 3%, in the values of the turbulence intensity from $Re = 100$ up to 110 is observed. From $Re = 110$ to 115 there is an increase of 25% in the values of the turbulence intensity, indicating acceleration in the trend towards stronger flow dynamics.

The transition on the flow regime clearly occurs at $Re = 120$, with the values of the turbulence intensity approximately doubling within a range of Reynolds number value of only five.

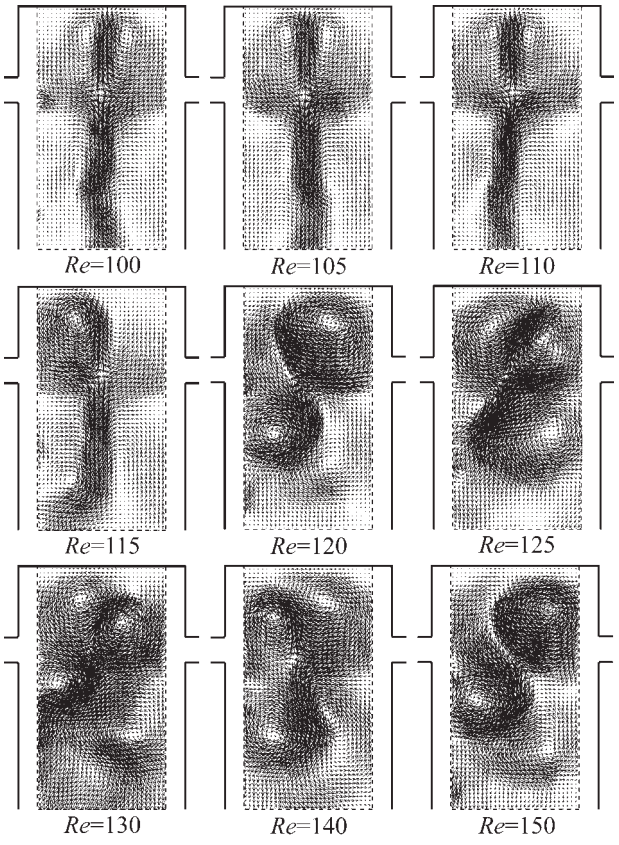

Figure 6. 2D instantaneous velocity vector maps for the experiments of Set 2 from *Re* = 100 to *Re* = 150.

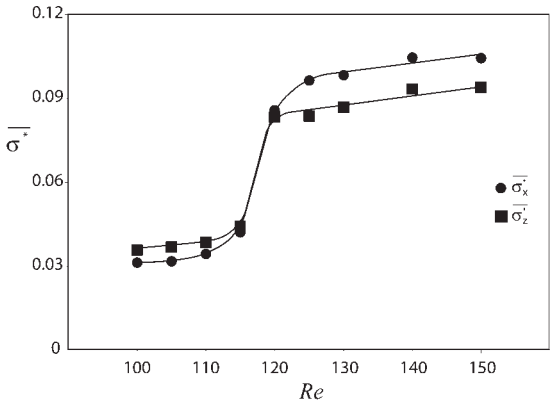

Figure 7. Plot of the variation of the *x* and *z* components of the average intensity of turbulence, σ_x^* and σ_z^*, with the Reynolds number for the Set 2 experiments.

The plot of $\overline{\sigma_x^*}$ and $\overline{\sigma_z^*}$ now proves that the long before known flow regime transition in the RIM mixing chamber,[10] occurs suddenly at the Reynolds number range of $115 \pm 10 \leq Re \leq 120 \pm 10$. Over this very short range of Reynolds numbers the $\overline{\sigma_x^*}$ and $\overline{\sigma_z^*}$ values are doubled. Although the transition occurs steeply, it is here shown that the instability in the system continuously growth with *Re* with an increasing growth rate up to $Re = 120$.

Local Variation of υ_x^* *PDF with Re*. For a greater insight of the flow-field changes at the critical Reynolds number, the values of the probability density functions, pdf, of υ_x^* were computed according to Eq. 11 at three points located along the chamber axis: $z = 5.0$, 7.5, and 10.0 mm. The locations of the three sampled points are shown in Figure 2, and the pdf's of υ_x^* at the three points are shown in Figure 8.

From the pdf's of υ_x^* it is clear that the amplitude of the lateral oscillations of the flow at the chamber axis dramatically increase from $Re = 115$ to $Re = 120$. From $Re = 100$ to 115 there is a slight increase in the amplitude of υ_x^* oscillations, which is seen from the higher probability of finding nonzero values of υ_x^* along the chamber axis. This trend is more clearly seen in the points further downstream the impingement point, at $z = 10.5$ mm, where in the pdf of υ_x^* the higher spread of values around zero for $Re = 115$, in comparison to $Re = 100$, is clear than at $z = 7.5$ mm. The small increase in the jets oscillations at the impingement point are thus being propagated and magnified to positions downstream the chamber.

It is most likely that the opposite process of the propagation of the stronger oscillations to upstream until the impingement point plays a key role in the ignition of a fully developed chaotic flow regime. Further proof of that maybe found in the work of Santos[28] where it was seen that the formation of vortices dictates the jets oscillation frequency. The basis of this phenomenon is probably the higher freedom of the flow to oscillate downstream the jets, since it is not so constrained by the jets that are two opposite well-balanced forces, and thus it is more likely that the oscillations grow stronger downstream and only afterwards affect the jets equilibrium.

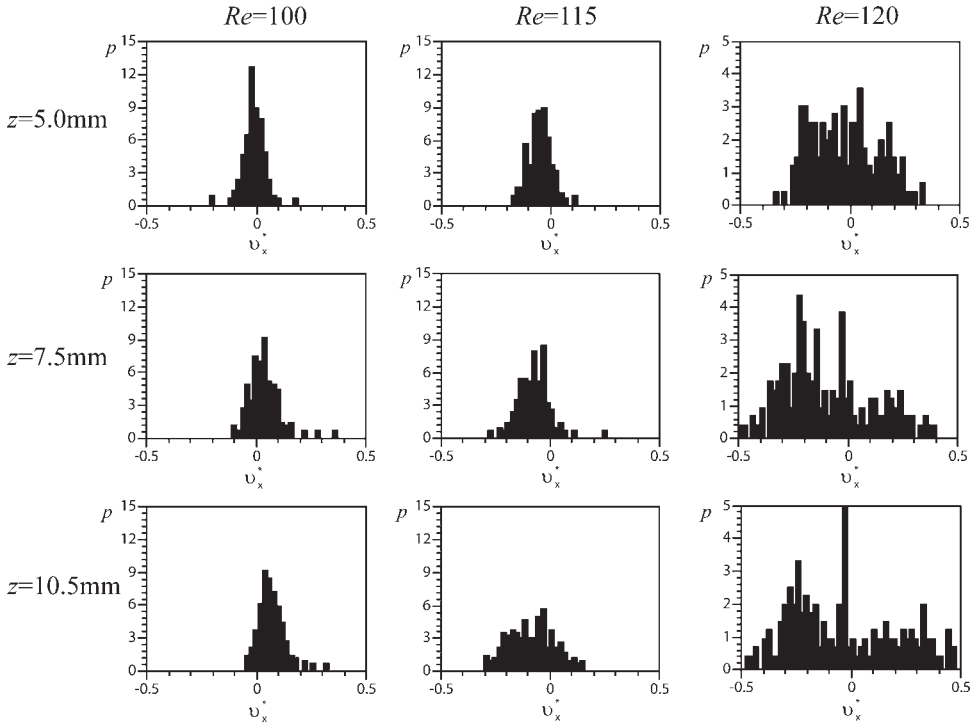

Figure 8. Plots of the pdf of υ_x^* for *Re* = 100, 115 and 120 in the points located at *x* = 0 and *z* = 5.0 mm, 7.5 mm and 10.0 mm, P1, P2, and P3, respectively, for the Set 2 experiments.

Conclusions

In this work the flow-field in the RIM mixing chamber was for the first time characterized from the instantaneous 2D maps of the velocity vector at the range of Reynolds numbers used in the industrial RIM processes. The present work was restricted to the plane containing the chamber and injectors axis, known from previous LDA results[8] to have the strongest flow dynamics. The complete imaging of the flow will require the study at different planes inside the mixing chamber, preferably resorting to 3D PIV.

The spatial distribution of the flow dynamics, here shown from its fluctuations by the turbulence intensity, was also mapped for the first time in the *xz* plane, completing the previous published results that focused in the *xy* plane.[8] The concentric distribution of the turbulence intensity, peaking at the jets impingement point, indicates that the instability generated from the opposition of two forces, the jets, is the main source of mixing in RIM.

From the thorough characterization of the flow-field in the range of Reynolds number marking the transition to self-sustainable chaotic regime, it was shown here that the flow instabilities are first generated downstream of the jets impingement point, prior to the actual flow regime transition.

This study has depicted the flow structures underlying the patterns observed in many mixing studies, giving a clear image of the mixing mechanisms in RIM. These results are also of outmost importance in the validation of results from CFD simulations that will be the basis of future enhancements in the RIM mixing chamber design.

Acknowledgments

Financial support for this work was in part provided by national research grant FCT/POCTI/EQU/345115/2000 and by LSRE financing by FEDER/POCI/2010, for which the authors are thankful. Ertugrul Erkoç acknowledges his Ph.D./scholarship by FCT (SFRH/BD/18901/2004). Ricardo J. Santos acknowledges financial support from POCI/N010/2006.

Notation

d = injectors diameter
D = chamber diameter
F_{pixel} = conversion factor between length in meters and pixels
h = distance of injectors axis from mixing chamber top
H = chamber height
p = probability density function
Re = Reynolds number
t = time
x,y,z = cartesian space coordinates
X = mass fraction

Greek letters

μ = viscosity
θ = temperature
ρ = density
σ = turbulence intensity
υ = velocity

Subscripts

glycerine = property of glyceine
inj = at the injectors
m = length in meters
pixels = length in pixels
F = frames
water = property of water

Superscripts

* = dimensionless

Literature Cited

1. Macosko CW. *RIM, Fundamentals of Reaction Injection Moulding*. Munich: Hanser, 1989.
2. Gobby D, Angeli P, Gavriilidis A. Mixing characteristics of T-type microfluidic mixers. *J Micromechan Microeng*. 2001;11:126–132.
3. Frouzakis CE, Tomboulides AG, Lee J, Boulouchos K. From diffusion to premixed flames in an H2/Air opposed-jet burner: the role of edge flames. *Combust Flame*. 2002;130:171–184.
4. Wehrmeyer JA, Cheng Z, Mosbacher DM, Pitz RW, Osborne R. Opposed jet flames of lean or rich premixed propane-air reactants versus hot products. *Combust Flame*. 2002;128:232–241.
5. Mahajan AJ, Kirwan DJ. Micromixing effects in a two-impinging-jets precipitator. *AIChE J*. 1996;42:1801–1814.
6. Johnson BK, Prud'homme RK. Chemical processing and micromixing in confined impinging jets. *AIChE J*. 2003;49:2264–2282.
7. Marchisio DL, Rivautella L, Barresi AA. Design and scale-up of chemical reactors for nanoparticle precipitation. *AIChE J*. 2006;52: 1877–1887.
8. Teixeira AM, Santos RJ, Costa MRPFN, Lopes JCB. Hydrodynamics of the mixing head in RIM: LDA flow-field characterisation. *AIChE J*. 2005;51:1608–1619.
9. Lee LJ, Ottino JM, Ranz WE, Macosko CW. Impingement mixing in reaction injection molding. *Polym Eng Sci*. 1980;20:868–874.
10. Tucker CL, Suh NP. Mixing for reaction injection molding. I. Impingement mixing of liquids. *Polym Eng Sci*. 1980;20:875–886.
11. Bierdel M, Piesche M. CFD—simulation and experimental investigation of impingement mixing in reaction injection molding (RIM). Paper presented at *3rd European Congress of Chemical Engineering*; 26–28 June 2001; Nuremberg.
12. Sandell DJ, Macosko CW, Ranz WE. Visualization technique for studying impingement mixing at representative Reynolds numbers. *Polym Process Eng*. 1985;3:57–70.
13. Wood P, Hrymak AN, Yeo R, Johnson DA, Tyagi A. Experimental and computational studies of the fluid mechanics in an opposed jet mixing head. *Phys Fluids A*. 1991;3:1362–1368.
14. Johnson DA, Wood P, Hrymak AN. The effect of geometrical parameters on the flow field of an opposed jet RIM mix head: equal flow and matched fluids. *Can J Chem Eng*. 1996;74:40–48.
15. Johnson DA, Wood P. Self-sustained oscillations in opposed impinging jets in an enclosure. *Can J Chem Eng*. 2000;78:867–875.
16. Santos RJ, Teixeira AM, Lopes JCB. Study of mixing and chemical reaction in RIM. *Chem Eng Sci*. 2005;60:2381–2398.
17. Santos RJ, Teixeira AM, Costa MRPFN, Lopes JCB. Operational and design study of RIM machines. *Int Polym Proc*. 2002;17:387–394.
18. Unger DR, Muzzio FJ. Laser-induced fluorescence technique for the quantification of mixing in impinging jets. *AIChE J*. 1999;45:2477–2486.
19. Unger DR, Muzzio FJ, Brodkey RS. Experimental and numerical characterization of viscous flow and mixing in an impinging jet contactor. *Can J Chem Eng*. 1998;76:546–555.
20. Zhao Y, Brodkey RS. Particle paths in three-dimensional flow fields as a means of study: opposing jet mixing system. *Powder Technol*. 1998;100:161–165.
21. Zhao Y, Brodkey RS. Averaged and time-resolved full-field (three-dimensional), measurements of unsteady opposed jets. *Can J Chem Eng*. 1998;76:536–545.
22. Hoffman M, Schlüter M, Räbiger N. Experimental investigation of liquid-liquid mixing in T-shaped micro-mixers using μ-LIF and μ-PIV. *Chem Eng Sci*. 2006;61:2968–2976.
23. Wong SH, Ward MCL, Wharton CW. Micro T-mixer as a rapid mixing micromixer. *Sens Actuators B*. 2004;100:359–379.
24. Liu Y, Fox RO. CFD predictions for chemical processing in a confined impinging-jets reactor. *AIChE J*. 2006;52:731–744.
25. Machuga SC, Midje HL, Peanasky JS, Macosko CW, Ranz WE. Microdispersive interfacial mixing in fast polymerizations. *AIChE J*. 1988;34:1057–1064.
26. Ranz WE. Analysis of reaction processes in which microscopic heterogeneities appear: scale-up and scale-down of polymerization reactions. *Ind Eng Chem Fundam*. 1986;25:561–565.
27. Malguarnera SC, Suh NP. Liquid injection molding I. An investigation of impingement mixing. *Polym Eng Sci*. 1977;17:111–115.
28. Santos RJ. *Mixing Mechanisms in Reaction Injection Moulding—RIM*. An LDA/PIV Experimental Study and CFD Simulation [PhD]. Porto: Faculdade de Engenharia da Universidade do Porto, 2003.
29. Westerweel J. Fundamentals of digital particle image velocimetry. *Meas Sci Technol*. 1997;8:1379–1392.
30. Huang H, Dabiri D, Gharib M. On errors of digital particle image velocimetry. *Meas Sci Technol*. 1997;8:1427.
31. Nogueira J, Lecuona A, Rodríguez PA. Data validation, false vectors correction and derived magnitudes calculation on PIV data. *Meas Sci Technol*. 1997;8:1493–1501.
32. Wang SJ, Mujumdar AS. Three-dimensional analysis of flow and mixing characteristics of a novel in-line opposing-jet mixer. *Ind Eng Chem Res*. 2007;46:632–642.
33. Trautmann P, Piesche M. Experimental investigation on the mixing behaviour of impingement mixers for polyurethane production. *Chem Eng Technol*. 2001;24:1193–1197.
34. Harris RF, Anderson RM, Shannon DM. Speciality polyurethane soft segments. II. Mixing studies in micro-RIM using polyether diamine oligomers containing backbone urea moieties. *J Appl Polym Sci*. 1992; 46:1547–1560.
35. Kusch HA, Ottino JM, Shannon DM. Analysis of impingement mixing-reaction data: use of a lamellar model to generate fluid mixing information. *Ind Eng Chem Res*. 1989;28:302–315.
36. Kolodziej P, Yang WP, Macosko CW, Wellinghoff ST. Impingement mixing and its effect on the microstructure of RIM polyurethanes. *J Polym Sci*. 1986;25:2359–2377.

Manuscript received Jun. 11, 2007, and revision received Jan. 16, 2008.